

Interference between the modes of an all-dielectric meta-atom

David A. Powell*

*Nonlinear Physics Centre and Centre for Ultrahigh-bandwidth Devices for Optical Systems (CUDOS),
Research School of Physics and Engineering, The Australian National University, Canberra, ACT 2601, Australia.*

The modes of silicon disk meta-atoms are investigated, motivated by their use as a building block of Huygens' metasurfaces. A model based on these modes gives a clear physical explanation of all features in the extinction spectrum, in particular due to the interference between non-orthogonal modes. By performing a vector spherical harmonic expansion of each mode, the complex features of the far-field scattering spectrum are also readily explained. It is shown that in general each mode has contributions from many multipole moments. Higher order modes with appropriate symmetry are also able to satisfy the Huygens condition, leading to multiple bands of strong forward scattering and suppressed back scattering. These results demonstrate a robust approach to find the modes of nano-photonic scatterers, commonly referred to as quasi-normal modes. By utilising an integral formulation of Maxwell's equations, the problem of normalising diverging far-fields is avoided. The approach is implemented in an open-source code.

I. INTRODUCTION

Dielectric resonators have applications in microwave and optical frequency ranges, including antennas¹ and as building blocks of impedance-matched Huygens' metasurfaces². Approximate methods for finding the modes of dielectric resonators are known³, which usually assume that $\epsilon \gg 1$. These methods are inaccurate for the moderate values of permittivity available at optical frequencies, and more sophisticated methods are needed to account for radiation effects. Open nanophotonic resonators such as meta-atoms, nano-antennas and oligomers are typically strongly radiative systems, where loss cannot be treated as a perturbation. Furthermore, in many nanophotonic systems, material dispersion and losses cannot be neglected, further complicating the problem of finding their modes.

In radiating and dissipative systems the modes have complex frequencies $j\omega_n + \Omega_n$, corresponding to damped oscillations of the form $\exp(\Omega_n t) \cos(\omega_n t)$, with $\Omega_n < 0$. The corresponding modal fields \mathbf{E}_n do not possess the orthogonality usually found in the modes of closed systems, and they are commonly referred to as quasi-normal modes⁴. They are particularly useful for solving dipole emission problems⁵, since they allow a mode volume to be defined for open cavities⁶. A significant practical difficulty is the requirement to normalise a mode with diverging far-fields⁷.

A different perspective on this problem can be found within the microwave engineering literature⁸, originally motivated by time-domain radar scattering problems. By using integral methods to solve Maxwell's equation, only currents on the scatterer need to be solved for, avoiding having to explicitly handle the diverging far-fields. As it is based on finding the singularities of a scattering operator, this approach is referred to as the singularity expansion method (SEM). The field distributions corresponding to these singularities are identical to the quasi-normal modes at the complex frequencies of the singularities $j\omega_n + \Omega_n$. When solving scattering prob-

lems on the $j\omega$ axis, the fields in the SEM approach are reconstructed from the dyadic Green's function, which remains finite in the far-field. Thus the SEM avoids the most significant practical disadvantage of quasi-normal modes based on fields.

Recently it has been shown that the singularity expansion method can be applied to meta-atoms and plasmonic resonators^{9–11}, clearly identifying the modes which contribute to scattering and coupling problems. However, finding all modes within a region of the complex frequency plane requires an iterative procedure with multiple contour integrations¹². This greatly increases the computational burden, and it remains unclear how robust this procedure is. In addition, it has not yet been demonstrated whether all spectral features can be explained by such a model, particularly the interference between non-orthogonal modes in the extinction spectrum and suppression of back-scattering corresponding to the Huygens condition¹³.

In this work, a robust integral approach to finding modes of open resonators is demonstrated for an all-dielectric meta-atom, based on the singularity expansion method. It is shown how this leads to a clear decomposition of the extinction spectrum of a silicon disk, automatically accounting for interference between the non-orthogonal modes. By performing a vector spherical harmonic decomposition of each mode, the unidirectional scattering behaviour of the disk is explained. It is shown that higher-order modes can also interfere to suppress back-scattering, corresponding to the previously reported generalized Huygens' condition¹⁴.

II. MODELLING APPROACH

A brief overview of integral equation methods to solve Maxwell's equations is given, followed by the robust approach to find the modes. Here dielectric objects are considered, and treated through a surface equivalent problem, with surface equivalent electric and magnetic currents, $\mathbf{J} = \mathbf{n} \times \mathbf{H}$ and $\mathbf{M} = -\mathbf{n} \times \mathbf{E}$, where \mathbf{n} is the surface

normal. These surface currents can be excited by the incident electric or magnetic field, yielding the electric field integral equation and magnetic field integral equation respectively. To yield a stable solution, both of these equations must be combined using some chosen weighting coefficients¹⁵. In this work the combined-tangential form is used, as detailed in Ref. 16. This gives us an operator equation relating equivalent surface currents to the tangential components of the incident fields

$$\mathcal{Z}(\mathbf{J}, \mathbf{M}) = (\mathbf{E}_{\text{inc}}, \mathbf{H}_{\text{inc}})|_{\text{tan}} \quad (1)$$

In this work the time convention $\exp(st)$ is used, with $s = j\omega + \Omega$. Note that in contrast to other conventions, the imaginary part gives the oscillation rate, and the real part gives the decay rate. We could find the corresponding time-domain function $f(t)$ of a frequency-domain function $f(s)$ through the inverse Laplace transform $f(t) = \mathcal{L}^{-1}\{f(s)\}$. Physically observable quantities must be represented by a real function in the time domain, thus they must satisfy the constraint $f(s^*) = f^*(s)$ in the frequency domain.

Equation (1) is solved using the boundary element method (also known as the method of moments¹⁷). After choosing sets of basis functions $\mathbf{f}(\mathbf{r})$ and testing functions $\mathbf{g}(\mathbf{r})$ (both are loop-star functions¹⁸ in this work), the operator equation becomes a finite-dimensional matrix equation

$$\mathbf{V}(s) = \mathbf{Z}(s) \cdot \mathbf{I}(s), \quad (2)$$

where \mathbf{I} is the vector containing the weighted equivalent surface currents

$$I_k = \left[\int \mathbf{f}_k(\mathbf{r}) \cdot \mathbf{J}(\mathbf{r}) d^2\mathbf{r}, \frac{1}{\eta_0} \int \mathbf{f}_k(\mathbf{r}) \cdot \mathbf{M}(\mathbf{r}) d^2\mathbf{r} \right]^T, \quad (3)$$

and \mathbf{V} is the source vector containing the projected incident fields

$$V_k = \left[\int \mathbf{g}_k(\mathbf{r}) \cdot \mathbf{E}_{\text{inc}}(\mathbf{r}) d^2\mathbf{r}, \eta_0 \int \mathbf{g}_k(\mathbf{r}) \cdot \mathbf{H}_{\text{inc}}(\mathbf{r}) d^2\mathbf{r} \right]^T. \quad (4)$$

The impedance matrix $\mathbf{Z}(s)$ is dense and frequency dependent, and contains all information regarding the response of the scatterer to arbitrary incident fields. The unknown current vector \mathbf{I} is solved for a given incident field vector \mathbf{V} , with the solution is given by $\mathbf{I} = \mathbf{Z}^{-1} \cdot \mathbf{V}$. The singularities of $\mathbf{Z}^{-1}(s)$ will dominate the spectrum of the response, and by Mittag-Leffler's theorem the response may be expanded in terms of these singularities¹⁹. They correspond to solutions which can exist in the absence of a source, and hence they can be used to model the response to an arbitrary incident field.

A. Finding modes

The most important singularities of the impedance matrix are its poles, corresponding to the quasi-normal

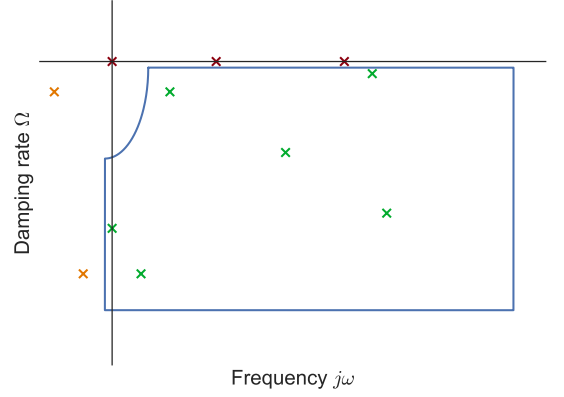


FIG. 1. Modes are found using a contour integration in the complex plane, which yields all enclosed poles $s_n = j\omega_n + \Omega_n$ and their residues with only a single integration. Green crosses: physical modes with finite radiation damping. Red crosses: spurious internal solutions with no damping. Orange crosses: conjugate modes which can be found by symmetry.

modes of the system. In practice it may usually be assumed that all poles are of first order²⁰. The poles correspond to frequencies $s_n = j\omega_n + \Omega_n$, satisfying $\mathbf{Z}(s_n) \cdot \mathbf{I}_n = 0$ and $\mathbf{K}_n \cdot \mathbf{Z}^T(s_n) = 0$ for non-zero \mathbf{I}_n and \mathbf{K}_n . These are the left and right eigenvectors of the system respectively, with \mathbf{I}_n being the surface current distribution of the mode.

The singularities of the impedance matrix are found by the contour integration procedure outlined in Ref. 21. First a pair of matrix integrals $\mathbf{C}_1 = \oint \mathbf{Z}^{-1}(s) ds$ and $\mathbf{C}_2 = \oint s \mathbf{Z}^{-1}(s) ds$ is evaluated about a contour containing all modes of interest, as shown schematically in Fig. 1. The contour is offset slightly from the $j\omega$ axis to eliminate any modes which do not couple to incident radiation, hence have $\Omega_n = 0$. The desired radiating modes are shown by green crosses, and have $\Omega_n < 0$. Since currents must be real functions in the time domain, for each pole there is a corresponding complex conjugate pole at $-j\omega_n + \Omega_n$, shown in orange. As the poles and residues are just complex conjugates of those with positive $j\omega_n$, they can be found by symmetry, and do not need to be included within the contour. Note that some poles are over-damped, with $j\omega_n = 0$, and these poles do not appear in conjugate pairs. The contour incorporates the $j\omega = 0$ axis in order to capture these poles. An arc is used to eliminate spurious numerical poles which cluster near the origin when using integral operators of the first kind²².

The mode frequencies and currents are eigenvalues and eigenvectors of $\mathbf{C}_2 \cdot \mathbf{I}_n = s_n \mathbf{C}_1 \cdot \mathbf{I}_n$. A singular value decomposition is used to determine the number of valid solutions to this equation²¹ and solving for the corresponding left eigenvalue problem yields the projectors \mathbf{K}_n . This procedure can yield solutions lying both inside and outside the contour, and those falling outside the contour are discarded. The poles and currents are

further improved by Newton iteration, then normalised so that $\mathbf{K}_n \cdot \mathbf{Z}'(s_n) \cdot \mathbf{I}_n = 1$. This ensures that the dyadic product of the eigenvectors matches the pole residue, i.e.

$$\mathbf{Z}(s) = \frac{\mathbf{I}_n \mathbf{K}_n}{s - s_n}, \quad (5)$$

in the vicinity of s_n , simplifying the pole expansion. Note that in general no orthogonality relation exists between these mode currents. As is discussed in Appendix B, orthogonality is not required for this approach. It will be shown how this non-orthogonality leads to physically meaningful interference effects.

Due to geometric symmetry, many modes are degenerate, with several different eigenvectors having the same pole location s_n . When solving the structure numerically, the imperfect symmetry of the mesh usually results in some frequency splitting of these degenerate modes, so a thresholding procedure is used to group closely spaced poles. The contour integration and iterative search procedure were found to cope with these nearly degenerate poles without requiring any special handling. Note that it is not necessary to orthogonalise degenerate modes, since the method is intrinsically able to account for non-orthogonality, as long as the modes span the full eigenspace.

B. Expanding currents in terms of modes

Once the modes have been found, currents can be solved for arbitrary incident fields,

$$\mathbf{I}(j\omega) = \sum_n \mathbf{I}_n \left(\frac{1}{j\omega - s_n} + \frac{1}{s_n} \right) \mathbf{K}_n \cdot \mathbf{V}(j\omega), \quad (6)$$

where we consider excitation at physically realisable frequencies on the $j\omega$ axis. The projector \mathbf{K}_n operates on the incident field \mathbf{V} to give its overlap with the mode. The bracketed term accounts for close the excitation frequency is to the mode's resonant frequency. Note that this polynomial has the correct asymptotic behaviour, thus improving the convergence and removing the need to include an entire function contribution¹⁹. The important result obtained from Eq. (6) is a scalar weighting of each mode's current vector \mathbf{I}_n .

Regardless of whether it is calculated directly from Eq. (2) or as a superposition of modes from Eq. (6), the current vector \mathbf{I} can be used to find the currents at any point on the surface. The dyadic Green's function can be then be used to find the fields anywhere in space. In practice this is not usually necessary, since many quantities of physical interest such as scattering, radiation forces and torques can be calculated directly from the currents²³. The quantity of most interest is the extinction cross-section

$$\sigma_{\text{ext}} = \mathbf{V}^*(j\omega) \cdot \mathbf{I}(j\omega) \eta_0 / |E_0|^2, \quad (7)$$

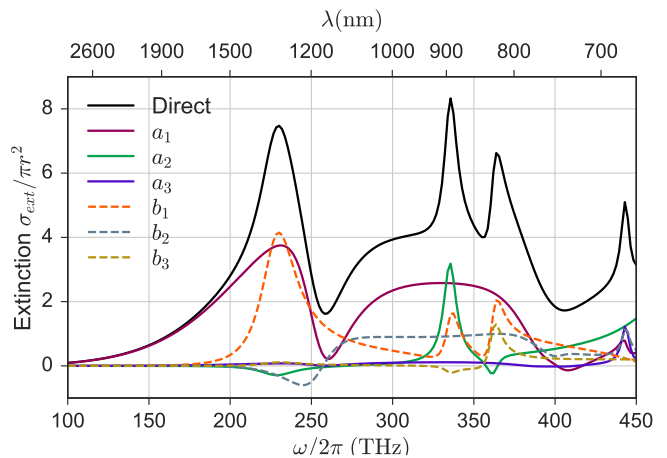


FIG. 2. The extinction cross-section of the the disk, direct calculation given by solid black line. Also shown is contributions from electric (solid) and magnetic (dashed) multipole moments. Curves are shown for different values of multipole order l , summed over all values of azimuthal index m .

giving the total work done by the incident fields on the currents. Here $|E_0|$ is the electric field of the incident plane-wave. This quantity can be defined for each mode by substituting the mode's current and its weighting from Eq. (6).

III. SILICON DISKS

The techniques outlined in Section II are now applied to study the scattering behaviour of a silicon disk meta-atom. As a first step, the structure is modelled directly without considering the modes, using Eq. (2). The radius is taken as 242 nm, height 220 nm and edges are rounded with radius 50 nm. The material properties of silicon were obtained by fitting an 8 pole model to the experimental data from Ref. 24. In Fig. 2 the extinction cross-section of the disk is plotted. The incident wave-vector is parallel to the axis of the disk.

As a first attempt to explain the spectral features, a multipole expansion is also shown in Fig. 2. Details of the expansion are given in Appendix A. Solid lines show the electric multipole moments a_l , and dashed curves show the magnetic moments b_l . Although the multipoles accurately reproduces the total extinction, there is no direct correspondence between modes and multipoles, with each peak exhibiting contributions from many multipole moments. Furthermore, several multipole moments show peaks and dips at similar locations, but it is unclear if these moments are linked to each other. Therefore *the multipole decomposition is unable to resolve the internal dynamics* which are observed in the extinction spectrum. It will be demonstrated that the model based on Eq. (6) can resolve these internal dynamics, showing which modes correspond to each of the spectral features.

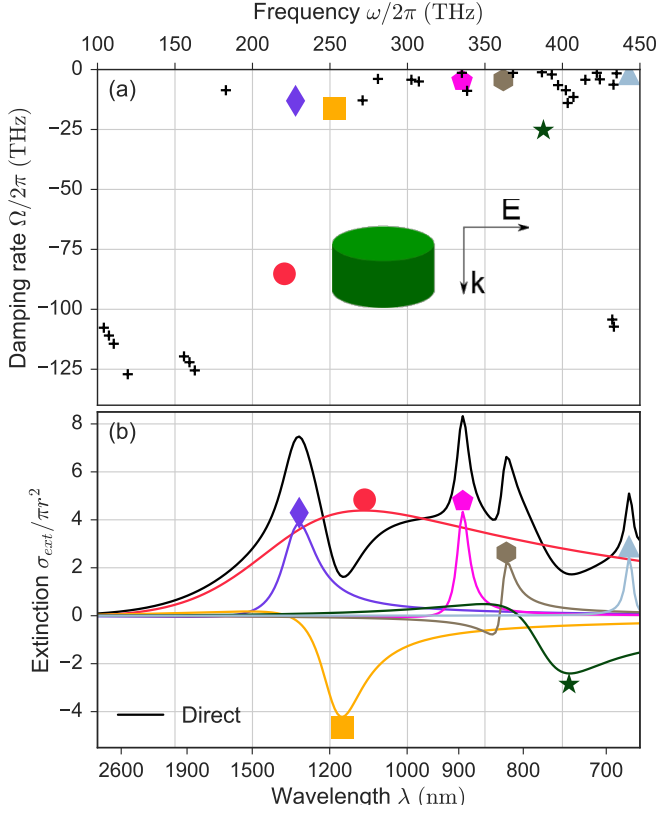


FIG. 3. (a) Poles of the silicon cylinder. Schematic shows the incident plane wave propagating along the cylinder axis. Coloured dots are the modes which couple strongly to the incident wave. (b) Directly calculated extinction (black), and contributions from each of the modes. Colors indicate correspondence between poles and extinction curves.

A. Modes of the silicon disk

The modes of the silicon disk are found by the procedure outlined in Section II A. Figure 3(a) shows the location of the poles in the complex frequency plane, with many of them being doubly degenerate. Since currents decay in time as $e^{\Omega t}$, more highly damped modes have more negative values of Ω_n . The schematic of the incident field orientation is shown in the inset. The modes which most strongly couple to this incident field are marked with coloured dots. The equivalent surface current \mathbf{J} of the first 5 of these modes is shown in Fig. 4. Note that these currents are complex, hence the plotted vectors give a snapshot of the oscillating current distribution. The divergence $\nabla \cdot \mathbf{J}$ is proportional to the equivalent surface charge (and hence to the normal component of the electric field) and is indicated by the shading of the surface. The colors of the markers next to each current distribution correspond to the poles shown in Fig. 3(a). Each mode is also given an arbitrary label in Roman numerals for reference purposes.

To understand the nature of these modes, we compare the disk with rounded edges to the sphere, since the two

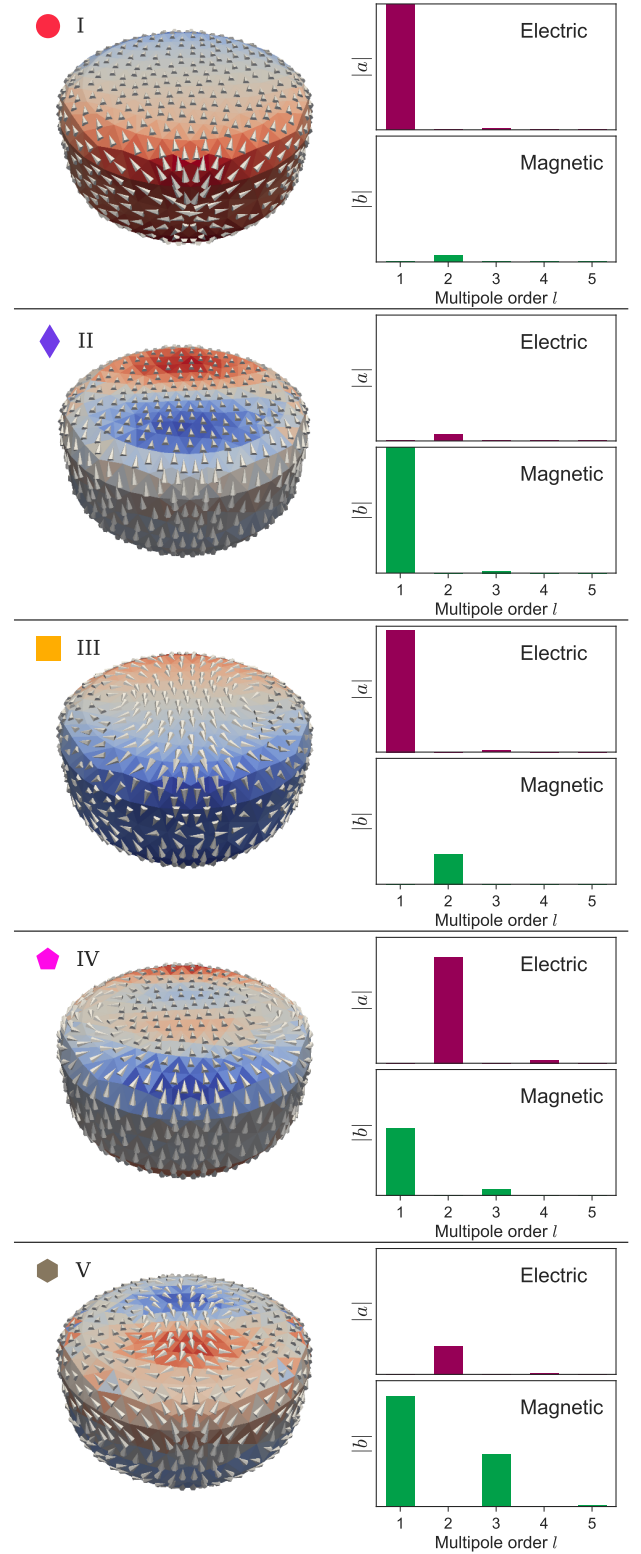


FIG. 4. Left: Modes of the disk, showing equivalent electric surface currents (arrows), and charges (colours). Markers correspond to poles in Fig. 3. Right: Spherical multipoles of each mode, scaled normalised according to the total scattered power.

are topologically equivalent. In Ref. 25, Sec. 9.22 it is shown that the poles of a sphere can be found from the roots of the denominators of the coefficients from Mie theory, involving spherical Bessel and spherical Hankel functions. The field corresponding to each of these poles is a pure vector spherical harmonic, with poles corresponding to radial index l having degeneracy of $2l + 1$. Note that for each vector spherical harmonic there is an infinite number of poles, corresponding to different number of radial oscillations inside the sphere²⁶.

We can consider the dielectric disk to be a sphere which has been transformed in a continuous manner, breaking the spherical symmetry. This means that the total number of poles is the same for both geometries, but the degeneracy is reduced by poles splitting to different locations. As a result, the corresponding current for each pole of the disk is not a pure vector spherical harmonic. By performing a multipole decomposition of the current for each mode of the disk, we can see which mode of the sphere it is most closely related to. This is shown in the right column of Fig. 4, where each mode's multipole moments are normalised to the total scattered power, as outlined in Appendix A. In all cases there is a single dominant multipole moment, although for higher order modes the influence of higher moments becomes more significant. In the following sections this multipole expansion of the modes will be used to explain their contributions to extinction and scattering.

B. Extinction spectrum

Figure 3(b) shows the extinction contribution from each of the modes, obtained from each term in Eq. (6). The extinction from degenerate pairs of modes has been combined, along with the contribution of their conjugate modes at $-j\omega_n + \Omega_n$. It can be seen that all features in the extinction spectrum can be clearly attributed to the modal contributions. The extinction spectrum for each mode exhibits only a single feature, being a peak and/or dip in the vicinity of its pole frequency ω_n . There is a very clear correspondence between the damping rate Ω_n and the sharpness of the features in the corresponding extinction curve. Note that for more highly damped modes, there is some shift between the peak and pole frequencies. This is because such modes couple strongly to the incident field, and therefore the overlap term in Eq. (6) can shift the spectral features away from the natural frequency $j\omega_n$. The accuracy and convergence of this model of extinction is shown in Appendix C.

One of the most striking features of Fig. 3(b) is that several modes show negative contributions to extinction. This is due to the non-orthogonality of the modes, which means that even if the incident field matches the profile of one mode, it may still excite others. It can be seen that the dip in extinction at around 260 THz can be attributed to a strong negative contribution from mode III, emitting radiation in the forward direction that is in-phase with

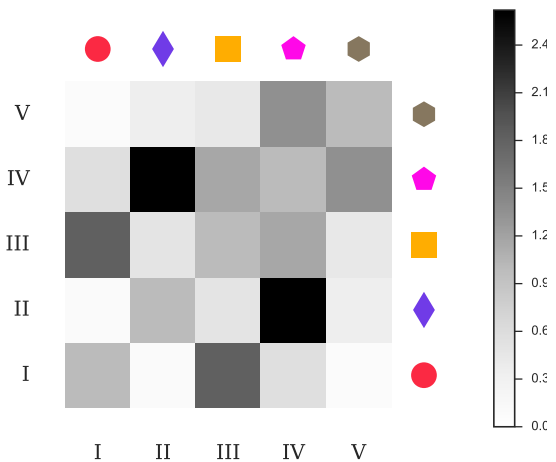


FIG. 5. Overlap integral between modes, illustrating their non-orthogonal nature. Mode numbers and symbols are listed on both x and y axes, and the corresponding shaded patch indicates the degree of mode overlap. Modes are normalised so that the self-terms on the diagonal axis are 1.

the incident field. In Ref. 27 it was shown how extinction can be decomposed into direct terms from each mode, plus interference terms between every pair of modes. The current obtained from Eq. (6) does not explicitly show separate direct and interference terms. Energy conservation dictates that the total extinction must be positive, so a sufficient set of modes must be included to have a physically meaningful result.

To quantify the interference between modes, their overlap $\mathbf{K}_n \cdot \mathbf{K}_m$ is plotted in Fig. 5, normalised such that $\mathbf{K}_n \cdot \mathbf{K}_n = 1$. This indicates how strongly an incident field having the shape of mode m excites mode n . For example, we see strong overlap between modes I and III, showing that the field which excites mode III also strongly excites mode I. This leads to the strong negative extinction observed for mode III. The strong overlap of modes I and III is consistent with their multipole decomposition shown in Fig. 4, where both are dominated by the a_1 electric dipole term.

The strongest mode overlap observable in Fig. 5 is between modes II and IV, consistent with both having strong magnetic dipole moment b_1 . However this does not lead to strong interference in Fig. 3(b). The low damping rates of these modes seen in Fig. 3(a) results in narrow resonant peaks which have little overlap. A notable feature of Fig. 5 is that mutual overlap terms can be greater than self terms, a consequence of the unconjugated inner product which appears in the formalism. It should also be noted that similarities in the multipole decomposition of modes is not always a good predictor of their overlap. For example, modes II and V have both have dominant magnetic dipole moments b_1 , but nonetheless have relatively weak overlap observable in Fig. 5.

C. Total scattering

To calculate the total scattering cross section, vector spherical harmonics are used, since the total scattering is the incoherent sum of all multipole contributions, given by Eq. (A1). Figure 6 shows the contribution of each multipole coefficient to the scattering cross-section. As with the multipole extinction spectrum shown in Fig. 2, the features of the multipole scattering spectra are rather complex, but can be explained by considering the contributions of different modes. In the wavelength range above 1000 nm, corresponding to measured range in Ref. 2, it can be seen that the scattering is dominated by the electric dipole and magnetic dipole moments a_1 b_1 . The magnetic dipole moment can be attributed to the resonance of mode II, which has negligible contributions from other moments.

The electric dipole moment a_1 appears to have two distinct maxima in Fig. 6. From the coefficients shown in Fig. 4, it is clear that only modes I and III contribute to this dipolar scattering. From Fig. 3(b), we can see that mode I has a very broad resonance, while mode III has a much narrower resonance, with a negative contribution to extinction. This results in cancellation of electric dipole radiation, corresponding to an anapole distribution²⁸. This effect is typically explained in terms of a quasi-static electric dipole (a linear current distribution) interfering with a toroidal dipole (a poloidal current distribution). The surface currents shown in Fig. 4 are consistent with this explanation, however the explanation in terms of modes is more general, and does rely on any low frequency approximation. Indeed, in Ref. 28 it was shown that for spheres, this condition occurs when the contributions from the first and second a_1 modes cancel. The situation for the disk is similar, the difference being that the interfering modes I and III have additional contributions from other multipole moments.

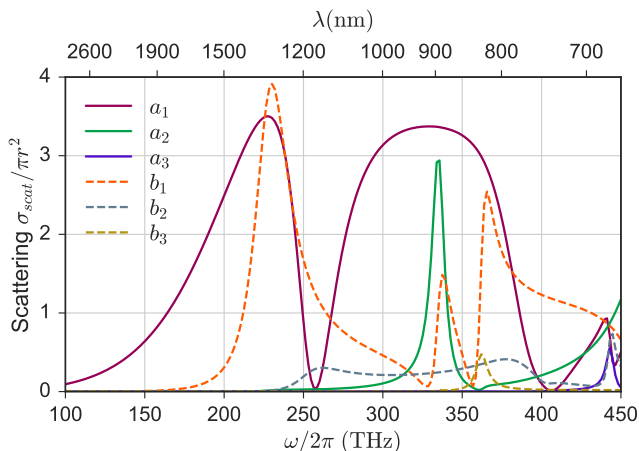


FIG. 6. Contribution of multipole moments to the scattering cross-section.

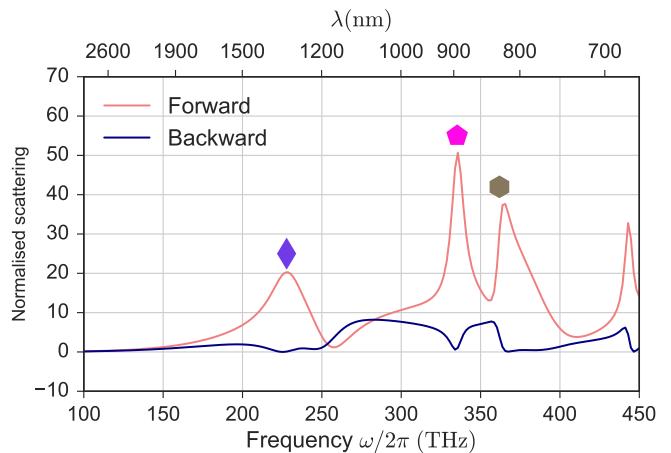


FIG. 7. Forward and backward scattering amplitudes. The markers indicate the modes corresponding to each of the peaks.

D. Directional scattering

For applications in Huygens' metasurfaces, the most important attribute of a meta-atom is to have suppressed back scattering and strong forward scattering. This is typically achieved by overlapping electric and magnetic dipole type resonances. Fig. 7 shows the forward and backward scattering amplitudes, with peaks labelled according to the corresponding resonant modes. The first peak of forward scattering corresponds to the overlap of modes I and III, with almost purely electric dipole radiation, and mode II, with almost purely magnetic dipole radiation.

It can also be seen that at the resonances of modes IV and V there are additional highly directional scattering features, as these modes also overlap with the electric-dipole type modes I and III. Examining the multipole decompositions in Fig. 4, it can be seen that mode IV is dominated by its electric quadrupole response, with a significant contribution from its magnetic dipole response. In contrast, mode V is dominated by its magnetic dipole response, with lesser contributions from electric quadrupole and magnetic octupole moments. It is significant that all of these multipole moments radiate anti-symmetric electric fields into the forward and backward directions. Thus all of these moments are able to cancel the electric dipole and magnetic quadrupole moments of modes I and III, which radiate with symmetric electric fields in the forward and backward direction.

Considering the contribution of modes to this directional scattering process, the generalised Huygens condition introduced in Ref. 14 can be re-interpreted as interference between modes of different symmetry. This suggests that to optimise this generalised Huygens' effect, the meta-atoms should be placed within a homogeneous dielectric environment, as has been done for all-dielectric Huygens' metasurface². A dielectric substrate without

a compensating superstrate introduces coupling between modes of opposite symmetry²⁹, greatly complicating the design process and degrading the directionality of scattering.

IV. CONCLUSION

A robust technique based on the singularity expansion method was presented to find the modes of a meta-atom, fully accounting for radiative losses. By solving Maxwell's equations using integral techniques, the normalisation of diverging fields typically required when using quasi-normal modes is avoided. The technique was applied to a silicon disk, a building block which enables optical metasurfaces having low loss, and full manipulation of the transmitted phase. It was demonstrated that the complicated features of the extinction spectrum can be readily explained in terms of contributions from the modes. Interference between non-orthogonal modes was shown to play a key role.

When considering far-field scattering properties, a vector spherical harmonic expansion yields an accurate, if somewhat opaque, description. By combining it with the modal analysis, the nature and origin of all scattering features can be elucidated. In the case of the silicon disk, there are several bands of strong forward scattering and suppressed backscattering, corresponding to the generalised Huygens' condition. It was shown that each band corresponds to the overlap of modes with odd and even radiation symmetry. The techniques used to find modes and construct models of scatterers are implemented in an open-source code OpenModes³⁰, along with notebooks to reproduce all results in this paper³¹.

ACKNOWLEDGMENTS

The author acknowledges useful discussions with Andrey Miroshnichenko, Sarah Kostinski, Mingkai Liu, and Yuri Kivshar. This research was funded by the Australian Research Council.

Appendix A: Multipole decomposition

The electric multipole coefficients a_{lm} and magnetic multipoles coefficients b_{lm} were computed directly from the surface currents using the formulas from Ref. 32. Duality allows these formulas to be generalised to include the equivalent magnetic currents through the substitution $\mathbf{J} \rightarrow j \frac{1}{\eta_0} \mathbf{M}$. The normalisation of multipole coefficients from Ref. 33 is used, as this simplifies the expression for scattering cross-section, which is given by

$$\sigma_{scat} = \frac{\eta_0}{k^2 |E_0|^2} \sum_{l=1}^{l_{max}} |a_l|^2 + |b_l|^2, \quad (\text{A1})$$

where the coefficients include contributions from all values of azimuthal index m :

$$|a_l|^2 = \sum_{m=-l}^l |a_{lm}|^2, \quad |b_l|^2 = \sum_{m=-l}^l |b_{lm}|^2. \quad (\text{A2})$$

In Fig. 4 $|a_l|^2$ and $|b_l|^2$ are normalised to their sum, and their square root is plotted since it more clearly shows the smaller contributions. In Fig. 6 these terms are plotted including the pre-factor from Eq. (A1) to give them dimensions of scattering cross-section.

For a plane wave propagating in the z direction, with incident electric field along the y direction, the extinction cross-section is given by³²

$$\sigma_{ext} = \frac{\pi}{k^2} \sum_{l=1}^{l_{max}} \sqrt{2l+1} \left(\left[\sum_{m=-1,1} \text{Im}\{a_{lm}\} \right] + \left[\sum_{m=-1,1} m \text{Im}\{b_{lm}\} \right] \right). \quad (\text{A3})$$

The quantities in square brackets are plotted in Fig. 2, including all common pre-factors in Eq. (A3). For 3 terms of the multipole expansion, the extinction plotted in Fig. 2 agrees with the direct calculation to a relative error below 2% for frequencies below 350THz.

By adapting the formulas from Mie theory³⁴, forward scattering can be found as

$$W_f = \frac{\pi}{4k^2} \left| \sum_{l=1}^{l_{max}} \sqrt{2l+1} \sum_{m=-1,1}^l a_{lm} + m b_{lm} \right|^2. \quad (\text{A4})$$

while back-scattering is given by

$$W_b = \frac{\pi}{4k^2} \left| \sum_{l=1}^{l_{max}} (-1)^l \sqrt{2l+1} \sum_{m=-1,1}^l a_{lm} - m b_{lm} \right|^2. \quad (\text{A5})$$

As losses are low in this system, the total extinction and scattering are approximately equal, due to the optical theorem. However, this still allows each multipole's contribution to extinction shown in Fig. 2 to be different from its contribution to scattering shown in Fig. 6.

Appendix B: Orthogonality of the modes

As discussed in Ref. 35, the electric fields of quasi-normal modes do not obey the usual orthogonality relationship based on a conjugated inner product, i.e. $\int \mathbf{E}_n^* \cdot \mathbf{E}_m d^3\mathbf{r} \neq \delta_{nm}$. However, they do obey an unconjugated orthogonality relationship, which is required for normalisation of modes⁷, and projection of external fields onto modal fields. In contrast, the current vectors on the scatterer obtained from the singularity expansion method do not exhibit any form of orthogonality. However, such orthogonality is not required when working with modal

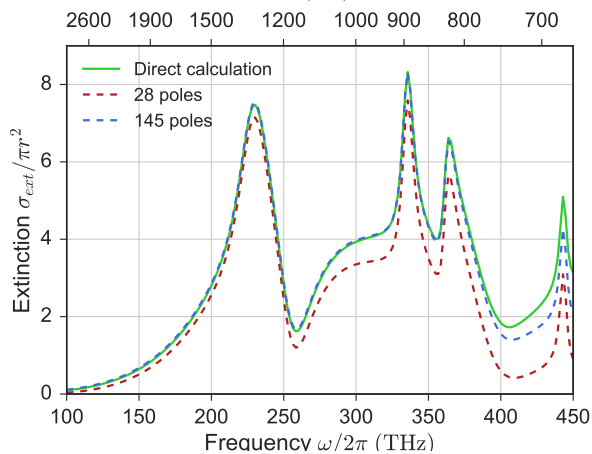


FIG. 8. Accuracy of the extinction calculated from modes (dashed lines), compared with directly calculated result (solid line).

currents, since they are normalised by weighting them to match the residue of the pole, as shown in Eq. (5). In addition to providing the current vector \mathbf{I}_n , this approach also yields the correctly normalised projector \mathbf{K}_n , which gives the projection of an arbitrary field onto each mode by a simple scalar product, as used in Eq. (6).

It is noted that in the literature a number of orthogonal decompositions of the impedance matrix \mathbf{Z} have been presented, most prominently the characteristic mode analysis³⁶. As these mode vectors are real, they exhibit the conventional conjugated orthogonality. However, such decompositions suffer from a number of problems which make them unsuited for physically modelling open resonators. First, the eigenvalue problem must be solved at each frequency, yielding a different set of current vectors at each frequency. This requires some algorithm to track modes with frequency³⁷, and effectively prevents their use in time-domain problems. More significantly, the enforcement of mode orthogonality on an inherently non-Hermitian system results in an artificial set of basis vectors which contain a complex mixture of underlying eigenvectors. This manifests itself in unphysical avoided crossings, whereby the nature of a pair of modes is swapped in some frequency region³⁸. The author has

observed similar behaviour when utilising other orthogonal decompositions of the impedance matrix, such as the singular value decomposition. In order to reproduce the interference phenomena observed in Fig. 3, it is essential to use the non-orthogonal modes obtained from singularity expansion method, or quasi-normal modes approaches.

Appendix C: Accuracy of the modal expansion

To confirm the accuracy of the mode expansion, the directly calculated extinction curve is plotted in Fig. 8 (solid line), as well as the sum of all contributions plotted in Fig. 3(b) (red dashed line). It can be seen that the agreement is good for frequencies below 250THz, however at high frequencies it becomes poorer. By increasing the number of poles considered from 28 (i.e. 7 modes, each doubly degenerate and with conjugate poles) to 145, much better agreement is achieved, as shown by the blue dashed curve. Clearly a model involving so many parameters is less useful as a design tool, thus there is an inevitable trade-off between accuracy and the level of insight provided. However, in contrast to simpler approaches based on point dipole or equivalent circuit models, it is possible to control the level of detail which is included within the model by choosing to include or exclude poles.

As this work includes materials with dispersion and dissipative losses, the impedance matrix $\mathbf{Z}(s)$ may exhibit branch point singularities, in addition to poles. The Green's function used to calculate elements of the impedance matrix has terms proportional to $\exp(-\gamma_0 r)$. The complex wave-number $\gamma_0 = \sqrt{\epsilon} \frac{s}{c}$ has branch points at the poles and zeros of the permittivity, connected by branch cuts^{11,39}. For the material data used in this work, all such branch points occur at frequencies above 800 THz, thus their contribution is neglected in Eq. (6). The accuracy of the results shown in Fig. 8 confirms that no significant contribution from branch points is missing from the result. The lack of branch points in the frequency range of interest also ensures that the integration contour illustrated in Fig. 1 does not intersect any of the branch cuts. Applying the contour integration in a frequency range of high dispersion would require choosing the contour so that it encircles branch points in pairs to avoid crossing branch-cuts.

* david.a.powell@anu.edu.au

¹ K. M. Luk, ed., *Dielectric Resonator Antennas*, Electronic & electrical engineering research studies Antenna series No. 11 (Research Studies Press, Baldock, 2003).

² M. Decker, I. Staude, M. Falkner, J. Dominguez, D. N. Neshev, I. Brener, T. Pertsch, and Y. S. Kivshar, *Advanced Optical Materials* **3**, 813 (2015).

³ J. Van Bladel, *IEEE Transactions on Microwave Theory and Techniques* **23**, 199 (1975).

⁴ E. Ching, P. Leung, A. Maassen van den Brink, W. Suen, S. Tong, and K. Young, *Reviews of Modern Physics* **70**, 1545 (1998).

⁵ P. T. Kristensen and S. Hughes, *ACS Photonics* **1**, 2 (2014).

⁶ C. Sauvan, J. P. Hugonin, I. S. Maksymov, and P. Lalanne, *Physical Review Letters* **110**, 237401 (2013).

⁷ P. T. Kristensen, R.-C. Ge, and S. Hughes, *Physical Review A* **92**, 053810 (2015).

- ⁸ C. E. Baum, Proceedings of the IEEE **64**, 1598 (1976).
- ⁹ X. Zheng, V. Volskiy, V. Valev, G. Vandenbosch, and V. Moschchalkov, IEEE Journal of Selected Topics in Quantum Electronics **19**, 4600908 (2013).
- ¹⁰ D. A. Powell, Physical Review B **90**, 075108 (2014).
- ¹¹ J. Mäkitalo, M. Kauranen, and S. Suuriniemi, Physical Review B **89**, 165429 (2014).
- ¹² X. Zheng, V. Valev, N. Verellen, V. Volskiy, L. Herrmann, P. Van Dorpe, J. Baumberg, G. Vandenbosch, and V. Moschchalkov, IEEE Photonics Journal **6**, 1 (2014).
- ¹³ C. Pfeiffer and A. Grbic, Physical Review Letters **110**, 197401 (2013).
- ¹⁴ S. Kruk, B. Hopkins, I. I. Kravchenko, A. Miroshnichenko, D. N. Neshev, and Y. S. Kivshar, APL Photonics **1**, 030801 (2016).
- ¹⁵ R. F. Harrington, Journal of Electromagnetic Waves and Applications **3**, 1 (1989).
- ¹⁶ P. Ylä-Oijala, M. Taskinen, and S. Järvenpää, Radio Science **40**, RS6002 (2005).
- ¹⁷ W. C. Gibson, *The Method of Moments in Electromagnetics* (Chapman & Hall/CRC, Boca Raton, 2008).
- ¹⁸ G. Vecchi, IEEE Transactions on Antennas and Propagation **47**, 339 (1999).
- ¹⁹ L. W. Pearson, Electromagnetics **1**, 395 (1981).
- ²⁰ L. Marin, Electromagnetics **1**, 361 (1981).
- ²¹ D. Bykov and L. Doskolovich, Journal of Lightwave Technology **31**, 793 (2013).
- ²² G. W. Hanson and A. B. Yakovlev, *Operator Theory for Electromagnetics* (Springer-Verlag, New York, NY, 2002).
- ²³ M. Reid and S. Johnson, IEEE Transactions on Antennas and Propagation **63**, 3588 (2015).
- ²⁴ M. A. Green and M. J. Keevers, Progress in Photovoltaics: Research and Applications **3**, 189 (1995).
- ²⁵ J. A. Stratton, *Electromagnetic Theory* (McGraw Hill, New York, 1941).
- ²⁶ M. I. Tribelsky and A. E. Miroshnichenko, Physical Review A **93**, 053837 (2016).
- ²⁷ B. Hopkins, A. N. Poddubny, A. E. Miroshnichenko, and Y. S. Kivshar, Physical Review A **88**, 053819 (2013).
- ²⁸ A. E. Miroshnichenko, A. B. Evlyukhin, Y. F. Yu, R. M. Bakker, A. Chipouline, A. I. Kuznetsov, B. Lukyanchuk, B. N. Chichkov, and Y. S. Kivshar, Nature Communications **6** (2015), 10.1038/ncomms9069.
- ²⁹ D. A. Powell and Y. S. Kivshar, Applied Physics Letters **97**, 091106 (2010).
- ³⁰ D. A. Powell, “OpenModes: An eigenmode solver for open electromagnetic resonators,” <http://davidpowell.github.io/OpenModes/>.
- ³¹ <https://github.com/DavidPowell/DielectricDiskPaper>, repository containing scripts to reproduce all figures in this paper.
- ³² P. Grahn, A. Shevchenko, and M. Kaivola, New Journal of Physics **14**, 093033 (2012).
- ³³ J. D. Jackson, *Classical electrodynamics*, 3rd ed. (John Wiley & Sons, 1999).
- ³⁴ C. F. Bohren and D. R. Huffman, *Absorption and Scattering of Light by Small Particles* (John Wiley & Sons, New York, 1983).
- ³⁵ P. T. Leung, S. Y. Liu, and K. Young, Physical Review A **49**, 3057 (1994).
- ³⁶ B. K. Lau, D. Manteuffel, H. Arai, and S. V. Hum, IEEE Transactions on Antennas and Propagation **64**, 2590 (2016).
- ³⁷ E. Safin and D. Manteuffel, IEEE Transactions on Antennas and Propagation **64**, 2628 (2016).
- ³⁸ K. R. Schab, J. M. Outwater, M. W. Young, and J. T. Bernhard, IEEE Transactions on Antennas and Propagation **64**, 2617 (2016).
- ³⁹ M. Mansuripur, M. Kolesik, and P. Jakobsen (2016) pp. 99310B–99310B–20.